Digital filters for low-latency quantification of brain rhythms in real time

To cite this article: Nikolai Smetanin *et al* 2020 *J. Neural Eng.* **17** 046022

Journal of Neural Engineering

PAPER

Digital filters for low-latency quantification of brain rhythms in real time

Nikolai Smetanin, Anastasia Belinskaya, Mikhail Lebedev and Alexei Ossadtchi

Center for Bioelectric Interfaces, Higher School of Economics, Moscow, 101000, Russia

E-mail: n.m.smetanin@gmail.com, belinskaya.anastasy@gmail.com, mikhail.lebedev@gmail.com and ossadtchi@gmail.com

RECEIVED
29 November 2019

REVISED
23 March 2020

ACCEPTED FOR PUBLICATION
14 April 2020

PUBLISHED
29 July 2020

Keywords: brain-state contingent paradigm, closed-loop neuroscience, neurofeedback, brain rhythm, envelope, instantaneous phase, feedback latency, state-dependent stimulation, optimal filtering, Hilbert transform, complex-valued filter, prediction

Abstract

Objective. The rapidly developing paradigm of closed-loop neuroscience has extensively employed brain rhythms as the signal forming real-time neurofeedback, triggering brain stimulation, or governing stimulus selection. However, the efficacy of brain rhythm contingent paradigms suffers from significant delays related to the process of extraction of oscillatory parameters from broad-band neural signals with conventional methods. To this end, real-time algorithms are needed that would shorten the delay while maintaining an acceptable speed-accuracy trade-off. *Approach.* Here we evaluated a family of techniques based on the application of the least-squares complex-valued filter (LSCF) design to real-time quantification of brain rhythms. These techniques allow for explicit optimization of the speed-accuracy trade-off when quantifying oscillatory patterns. We used EEG data collected from 10 human participants to systematically compare LSCF approach to the other commonly used algorithms. Each method being evaluated was optimized by scanning through the grid of its hyperparameters using independent data samples. *Main results.* When applied to the task of estimating oscillatory envelope and phase, the LSCF techniques outperformed in speed and accuracy both conventional Fourier transform and rectification based methods as well as more advanced techniques such as those that exploit autoregressive extrapolation of narrow-band filtered signals. When operating at zero latency, the weighted LSCF approach yielded 75% accuracy when detecting alpha-activity episodes, as defined by the amplitude crossing of the 95th-percentile threshold. *Significance.* The LSCF approaches are easily applicable to low-delay quantification of brain rhythms. As such, these methods are useful in a variety of neurofeedback, brain-computer-interface and other experimental paradigms that require rapid monitoring of brain rhythms.

1. Introduction

Investigations of neural oscillations have been and continue to be an area of intensive research, particularly with the advancement of neuroimaging techniques, such as noninvasive electroencephalography (EEG) and magnetoencephalography (MEG), invasive electrocorticography (ECoG) and stereo EEG (sEEG). Many experimental paradigms and methods have been developed in order to deal with specific types of neuronal oscillations particularly, experimental and clinical approaches for either enhancing or suppressing various brain rhythms [1, 2]. Existing paradigms for exploration of oscillatory activity fall in one of the two categories: (1) studies where stimuli are presented regardless of the specifics of the ongoing neural activity and (2) studies implementing a closed-loop design where the stimuli formation depends on the characteristics of the ongoing brain activity [3]. In this paper, we evaluate signal processing methods that are useful for the second category where the closed-loop is formed on the basis of the oscillatory activity quantified in real-time. We refer to this experimental approach as brain-rhythm contingent paradigm (BRCP) .

As shown in figure 1(A), BRCP operates via three key steps: (1) data acquisition, (2) target signal extraction, and (3) stimulus generation. During the data

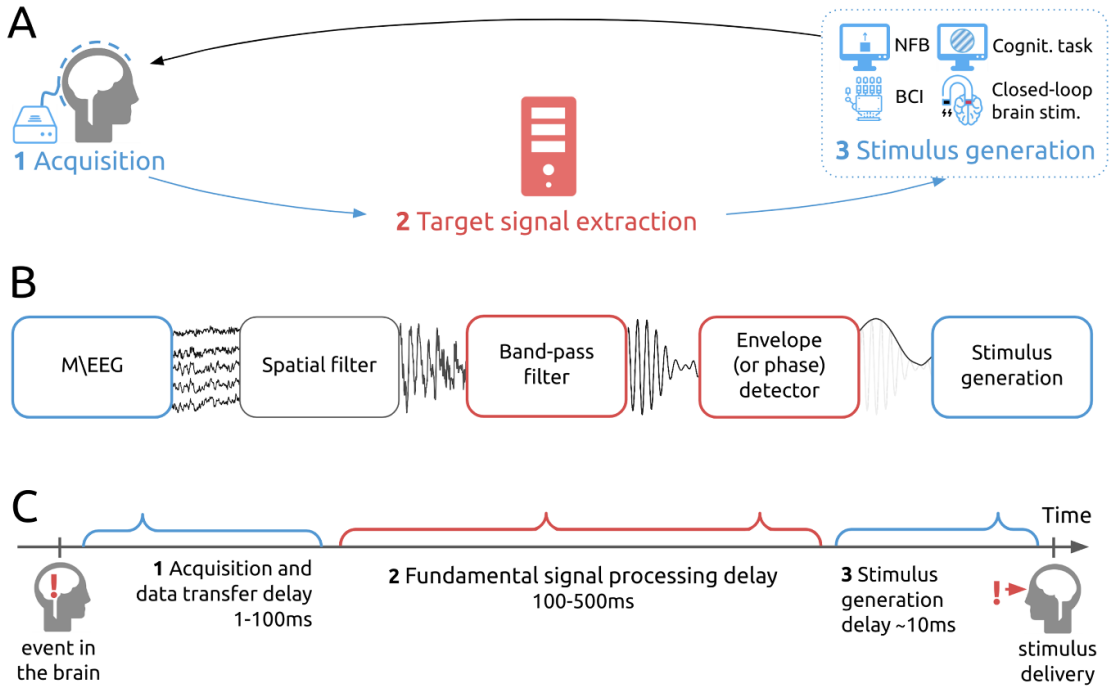

Figure 1. Schematics of BRCP. (A) Signal flow diagram in the closed-loop BRCP system (B) Signal processing pipeline (C) The sources of delays contributing to the total latency of BRCP. Delays with technical and fundamental sources are marked in blue and red, respectively.

acquisition step, brain activity is measured, usually with multiple spatially distributed electromagnetic sensors, and streamed to a computer. Within the target signal extraction step, a computer routine extracts the parameters of oscillatory activity from the multichannel data in real-time, typically amplitude and phase. At the stimulus generation step, these parameters are converted into a feedback delivered to the brain either directly, using stimulation applied to the nervous tissue (also called neuromodulation), or using natural senses: vision, hearing or touch. The feedback can be presented continuously and modulates the parameters of an ongoing stimulation, or discretely and contributes to selecting a stimulus from a predefined set.

Many implementations of BRCP have been developed allowing us to explore a variety of goal-directed behaviors dependent on a closed-loop design [3]. The most distinct versions of BRCP are: neurofeedback [4–7], brain computer interface (BCI) [8–10], closed-loop brain stimulation [11–13], and brain state-contingent stimulus delivery [14–20]. As such, BRCPs are applicable to the treatment of a range of neurological disorders [21], [22], cognitive enhancement therapy [23], and post-stroke rehabilitation [9], [10], [24]. Additionally, brain-state contingent stimulus presentation can reduce the overall session duration and reduce participants' fatigue, particularly when neural patterns of interest consist of short-lived episodes of activity [25, 26]. Despite the conceptual differences between the implementations of BRCP reported in the literature, their signal processing pipelines have many common features, as depicted in figure 1(B). The generic pipeline incorporates the spatial and temporal filtering steps in order to emphasize specific neural sources and frequency components, respectively. These filtering steps are often followed by quantification of the oscillatory envelope and phase.

Here we focus primarily on the multichannel recording methods with millisecond-scale temporal resolution, such as EEG and MEG. These techniques allow for exploration of the fine rhythmic structure of brain activity and, in principle, can enable closed-loop, instantaneous interaction with brain circuits. Yet, as explained in detail below, time-lags of both technical and fundamental nature occur during the online extraction of oscillatory parameters from the ongoing brain activity. These delays vary, depending on the concrete implementation and can be significantly reduced with the use of optimized signal processing methods.

Temporal specificity of BRCP is characterized by the overall delay between the onset of the neural event of interest and the time the corresponding feedback is issued (figure 1(C)). This overall BRCP latency incorporates time-lags related to different factors, some of them technical (i.e. software and hardware delays), others, fundamental (i.e. required to collect a sufficient amount of neural data to isolate a rhythmic component). The technical time-lags typically do not exceed 100 ms; this time is needed for data

transmission by the hardware and low-level software processing. These delays can be reduced by specific hardware and software solutions. From our experience, it is feasible to reduce the technical delay to 10–30 ms depending on the feedback delivery specifics. The fundamental lag cannot be reduced as easily because it is composed of the time needed to collect a snapshot of neural oscillatory data that could be then quantified with an appropriate algorithm like band-pass filtering and envelope/phase analysis. As such, this lag is fundamental: a longer observation time is required to improve the resolution over spectral frequencies. Suboptimal approaches used for extracting the envelope and/or phase of rhythmic neural components may mount to several hundreds of milliseconds of fundamental delay. This is undesirable in most closed-loop paradigms [27].

The adverse effect of feedback delays was reported in many neurofeedback applications and the BCI studies where participants were supposed to learn to modulate their own brain activity - with or without a mental strategy recommended by the experimenter [28]. A similar problem with long feedback delays was highlighted in several studies on evidence-based learning. Thus, back in 1948, Grice showed that learning to discriminate complex visual patterns drastically depends on the feedback signal latency [29]. Impaired performance caused by delayed feedback was also demonstrated in the studies on motor learning, e.g in the prism adaptation task [30]. According to Rahmandad *et al* [20], behavioral learning is impaired when feedback delay is misperceived by a participant. Moreover, an elongated feedback delay impairs the sense of agency during the BCI control [31], the finding also corroborated by the simulation study [32] showing that feedback delay and temporal blur adversely influence automatic (strategy free) learning in BCI tasks.

Temporal specificity is also an important consideration for the experimental settings with closed-loop brain stimulation and brain state triggered stimulus delivery [13, 33, 34]. Indeed, a key requirement for these methods is an accurate estimation of instantaneous oscillatory features and the timely delivery of stimuli to efficiently interfere with oscillatory neural patterns.

In the present study, we evaluate several approaches aimed at reducing the delay between neuronal events and the corresponding feedback in BRCP. We pay special attention to a family of methods based on the least-squares complex-valued filter (LSCF) design methodology to identify finite impulse response (FIR) filter weights and explicitly control the processing latency. The proposed approach is capable of extracting the instantaneous amplitude and phase of neural oscillations with a shorter latency and higher accuracy as compared to other techniques. With LSCF, the user can explicitly specify the desired delay which facilitates a flexible control of the speed-accuracy trade-off in the closed-loop neuroscientific experiments. .

2. Methods

Our basic assumption is that the measured neural activity $x[n]$ is a sum of the narrow-band signal $s[n]$ (neural activity targeted by a BRCP) and colored broad-band noise $\eta[n]$.

$$x[n] = s[n] + \eta[n] \tag{1}$$

The narrow band neural activity $s[n]$ utilized in a BRC paradigm can be represented as the real part of analytic signal $y[n]$ [35]:

$$y[n] = s[n] + js_h[n] = a[n]e^{j\phi[n]} \tag{2}$$

where $s_h[n]$ is the imaginary part of the analytic signal (often called second quadrature of the original signal), $a[n]$ is the instantaneous amplitude of the narrow band process at time n, and $\phi[n]$ is its instantaneous phase at time n. Sequence $a[n]$, often called envelope, is a relatively smooth real-valued sequence that skirts the local peaks of a narrow-band process. Importantly, envelope $a[n]$ and phase $\phi[n]$ can be instantaneously computed from the complex-valued analytic signal $y[n]$ as

$$\begin{aligned} a[n] &= \sqrt{\Re\{y[n]\}^2 + \Im\{y[n]\}^2}, \\ \phi[n] &= atan\left(\frac{\Im\{y[n]\}}{\Re\{y[n]\}}\right) \end{aligned} \tag{3}$$

As illustrated in figure 2(A), analytic signal $y[n]$ can be computed from $x[n]$ using narrow-band Hilbert transform [35] through the following steps. First, the discrete Fourier transform (DFT) is applied to the data segment of $x[n]$. Then, the obtained DFT coefficients are masked so that the coefficients corresponding to the frequency band of interest (designated on the positive-frequency semi-axis) are doubled and the others are set to zero. Lastly, the inverse Fourier transform (iDFT) is applied to obtain $y[n]$. This approach will inevitably deliver inaccurate values of $y(n)$ for the beginning and the end of the data segment it is applied to. To avoid this distortion, the segment needs to be augmented with flanker data—a procedure that is impossible to conduct in real time where the data segment ends at the last sampled point. This is because obtaining the flanker in this case would require an extension into the unknown future. Unlike the real-time operations, $y[n]$ is estimated accurately when the data segment is extended with true flanker data in the offline analysis. Then, using equations (3)

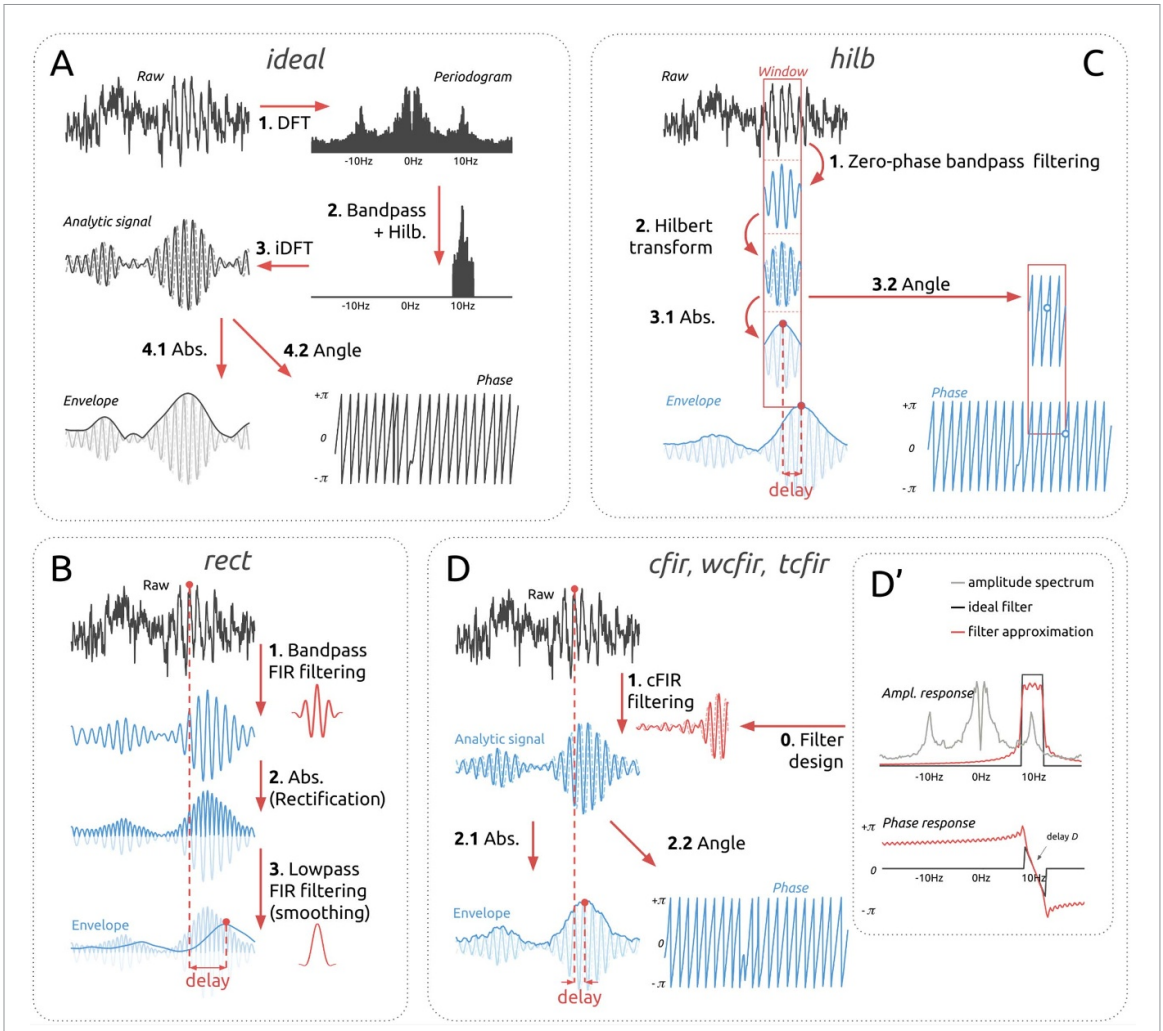

Figure 2. Methods for narrow-band signal envelope estimation. (A) Ideal non-causal system for ground truth signal extraction. (B) Envelope detector based on rectification of the band-filtered signal. (C) Sliding window narrow-band Hilbert transform-based method. (D) Complex-valued FIR family filters that perform FIR causal filter based approximation of the ideal non-causal system. (D') Complex-valued FIR filter design.

one can compute the ideal envelope $a[n]$ and phase $\phi[n]$ sequences. The rest of figure 2 shows a summary of the available causal techniques that can be applied in real-time to compute the envelope and instantaneous phase of a narrow-band component extracted from a broad-band signal.

2.1. Conventional methods

For didactic purposes, we start with the most basic approaches to extraction and quantification of the narrow-band processes.

2.1.1. Rectification and smoothing of the band-filtered signal (rect)

This is conceptually the most straightforward way to estimate the envelope $a[n]$. With this method, low-pass filtering is applied to the rectified narrow-band filtered signal, as illustrated in figure 2(B). This approach can be mathematically expressed as:

$$a_r[n] = h_{lp}[n] * \left| h_{bp}[n] * x[n] \right| \tag{4}$$

where $*$ is the convolution operator, h_{bp} is the impulse response of the band-pass filter, $|\cdot|$ denotes the absolute value (i.e. the rectification step), and h_{lp} is the impulse response of the low-pass filter that performs smoothing of the rectified signal. Without loss of generality, we can assume that both h_{bp} and h_{lp} are linear phase FIRs designed by a Hanning window method with the number of taps N_{bp} and N_{lp}, correspondingly. The cutoff frequency for the low-pass filter f_c is set to correspond to one-half of the expected bandwidth of the narrow-band process, i.e. $f_c = (f_2 - f_1)/2$. FIR filters have a linear phase and therefore the total delay D and the number of taps in the individual symmetric filters N_{bp} and N_{lp} are related as:

$$D = \frac{N_{lp} - 1}{2} + \frac{N_{bp} - 1}{2} \tag{5}$$

It follows from equation (5) that a given value of D can be achieved for multiple selections of N_{lp} and N_{bp}. In order to ensure the best envelope reconstruction accuracy for a given group delay value D, we

used grid search over variable N_{bp} in our comparative analysis. The parameter N_{lp} then follows directly from (5). Since N_{bp} and N_{lp} are positive, this method can estimate the envelope values only for a positive delay.

2.1.2. Sliding window narrow-band Hilbert transform (hilb)

This is a second most commonly used method that is based on the use of the analytic signal $y[n]$ computed using Hilbert transform [35]. There are various implementations of this approach. In this paper, we resorted to the use of the windowed discrete Fourier transform (DFT). The DFT is calculated on each window of length N_t which is zero-padded to the length of N_f samples. We then proceed as in the ideal approach but after computing the inverse DFT we retain only the (N_t-D)-th element of the resultant complex-valued sequence as an estimate of the analytic signal with delay D. This filter performs two operations simultaneously: band-pass filtering and extracting the analytic signal. The analytic signal is then used to instantaneously estimate the oscillatory envelope and phase. This algorithm is illustrated in figure 2(C).

In matrix representation and using temporal embedding to form vector $\mathbf{x}[n]$, this can be represented as:

$$y_h[n] = \frac{2}{N_f} \cdot \mathbf{w}_{N_t-D}^H \mathbf{W}_{\Delta f} \mathbf{x}[n], \tag{6}$$

where vector $\mathbf{x}[n]$ contains the last N_t samples of $x[n]$, i.e. $\mathbf{x}[n] = [x[n], x[n-1], \ldots x[n-N_t+1]]^T$, $\mathbf{W}_{\Delta f}$ is the N_f-by-N_t modified DFT matrix with zeros in the k-th row for k outside of the range $[f_1 N_f/f_s,\ f_2 N_f/f_s]$, which corresponds to the band of interest $\Delta f = [f_1,\ f_2]$ and $\mathbf{w}_{N_t-D}^H$ is the Hermitian transposed (N_t-D)-th column of the DFT matrix.

The overall delay of this method is explicitly determined by parameter D. The parameters to be optimized in this method are window length N_t and zero-padded length of the signal N_f.

2.1.3. Sliding window Hilbert transform with autoregressive prediction of the narrow-band filtered signal (ffiltar)

This approach was proposed by Chen *et al* [33] and applied in brain rhythm contingent transcranial magnetic stimulation (TMS) [13]. In this method, the sliding window vector $\mathbf{x}[n]$ containing N_a last samples is forward-backward bandpass filtered. Then, flanker N_e samples are truncated to eliminate edge artifacts, and $2N_e$ samples are forward predicted by using an autoregressive (AR) model fitted to the immediately preceding $N_a - N_e$ samples. Finally, Hilbert transformation of the prediction is used to estimate the analytic signal with zero latency at $n = N_a - N_e + N_e = N_a$ corresponding to the central point of the extrapolated segment of length $2N_e$. In the original work, this value was used to determine the current phase that was then extrapolated for the next cycle to determine the time for stimulation. This approach was originally designed for $D = 0$, so we used it as a benchmark when we comparing the performance of different methods operating at zero latency.

Using matrix notation, we can formalize this method as follows.

$$y_p[n] = \frac{2}{N_f} \cdot \mathbf{w}_{N_a}^H \mathbf{W}_+ \mathcal{P}_{AR(p)} \left\{ \tilde{\mathbf{x}}[n] \right\} \tag{7}$$

where $\tilde{\mathbf{x}}[n]$ contains forward-backward filtered last N_a samples of the $x[n]$, $\mathcal{P}_{AR(p)}$ denotes AR model based prediction operation that augments the truncated data segment and adds $2N_e$ predicted samples by using a p-th order AR model, $\mathbf{W}_+$ is the N_f-by-(N_a+N_e) modified DFT matrix with zeroed rows corresponding to the range of negative digital frequency values $[-\pi, 0]$ and $\mathbf{w}_{N_a}^H$ is the Hermitian transposed N_a-th row of the DFT matrix. We used a Butterworth filter of the order k as the narrow-band filter for the forward-backward filtering part as suggested in [33].

One of the disadvantages of this approach is that it has multiple parameters that need to be adjusted to achieve the optimal performance. To attain the best performance in this study, we searched over the parameter grid composed of the following variables: AR order p, number of flanker samples N_e, and Butterworth filter's order k.

2.2. Least squares complex-valued filter (LSCF) design approach

In order to build the analytic signal $y[n]$ that corresponds to an estimate of narrow-band signal $s[n]$ extracted from the noisy broad-band measurements $x[n]$, one can apply the ideal narrow-band Hilbert transform filter [36, 37]. The complex-valued frequency response of this combined filter can be defined as:

$$H_D(e^{jw}) = \begin{cases} 2e^{-jwD}, w \in [w_c - \delta w, w_c + \delta w] \subseteq [0, \pi] \\ 0, otherwise \end{cases} \tag{8}$$

where $\delta w = 2\pi\delta f$ is half of the pass band width, and D is the group delay measured in samples. This filter is non-causal for any finite delay D and therefore it cannot be applied in real time. To reconstruct the analytic signal causally, one can find a causal complex-valued finite impulse response (FIR) filter $\mathbf{b} = \{b[n]\}$ of length N_t that approximates the ideal complex-valued frequency response $H_D(e^{jw})$ [38]. This filter can be then applied in real-time as $y_c[n] = x[n]^* b[n]$ using the convolution of $\mathbf{b}$ and $x[n]$, the procedure

that by design incurs a fixed processing delay of D samples.

Causal complex-valued FIR filter $b[n]$ can be established by solving the least squares optimization problem. Various definitions of the cost functions lead to different filters.

2.2.1. Frequency domain least squares (cfir)
This is the most straightforward approach to quantifying narrow-band components present in the data. The least squares filter design strategy consists of finding the complex-valued vector of the FIR filter weights $\mathbf{b}$ of length N_t that minimizes the L_2 norm between the FIR filter frequency response obtained by the DFT and the discrete appropriately sampled version $\mathbf{h}_D$ of an ideal response $H_D(e^{j\omega})$ in the frequency domain. To increase the frequency resolution, we use a truncated DFT-matrix $\mathbf{W}$ with the dimensions $N_f \times N_t$ ($N_f \geq N_t$). The use of transform matrix-based formulation of the DFT in this case is equivalent to the DFT of N_t samples long vector zero-padded to length N_f. Since $\mathbf{W^H W} = N_f\mathbf{I}$, the solution $\mathbf{b}_{cfir}$ of the normal equations for the optimization problem (2.2) can be found by a simple inverse DFT of the desired complex-valued characteristics of the narrow-band Hilbert transformer:

$$\mathbf{b}_{cfir} = \arg\min_{\mathbf{b}} ||\mathbf{Wb} - \mathbf{h}_D||_{L_2}$$

$$\mathbf{b}_{cfir} = \frac{1}{N_f}\mathbf{W^H h}_D \tag{9}$$

Equation (9) is similar to equation (6) but can be used with negative delays, $D \leq 0$. This simple method, however, does not take into account the second order frequency domain statistics of the target signal and could be further improved. Note that the *cfir* approach with parameters N_t, N_f and $D \geq 0$ matches the sliding window narrow-band Hilbert transform approach with the same parameters N_t, N_f and D.

2.2.2. Frequency domain weighted least squares (wcfir)
This is the method that optimizes the filter by constructing weights from the power spectral density of the input signal $x[n]$. We thus formulate the weighted frequency domain least squares design technique via optimization problem

$$\mathbf{b}_{wcfir} = \arg\min_{\mathbf{b}} ||\mathbf{S}_x^{1/2}(\mathbf{Wb} - \mathbf{h}_D)||_{L_2} \tag{10}$$

whose solution can be found by solving the normal equations:

$$\mathbf{b}_{wcfir} = \left(\mathbf{W^H S}_x\mathbf{W}\right)^{-1}\mathbf{W^H S}_x\mathbf{h}_D \tag{11}$$

where $\mathbf{S}_x$ is the diagonal matrix formed from the samples of the power spectral density of $x[n]$ estimated over the entire training data segment. Note that only $\mathbf{W^H W} = N_f\mathbf{I}$ remains true while $\mathbf{WW^H} \neq N_t\mathbf{I}$. Therefore, at the optimum $||\mathbf{Wb} - \mathbf{h}_D|| \neq 0$ and thus $\mathbf{b}$ is the least squares approximation of the ideal filter that can be computed even for negative D.

Panels D and D' of figure 2 illustrate *cfir* and *wcfir* approaches. The delay D corresponds to the slope of the phase response within the pass-band and theoretically can be set to an arbitrary value. The analytic optimization procedure then aims at finding such complex-valued vector of the FIR filter coefficients $\mathbf{b}$ for which the desired transfer function $\mathbf{h}_D$ is approximated optimally in the least squares or weighted least squares sense.

Conceptually, having in mind the two tasks of optimal envelope and instantaneous phase estimation we could have formulated two separate optimization problems and used two different sets of weights implementing two different band-pass complex-valued filters delivering optimal accuracy in estimation of envelope and phase approximation with the specified delay. In this case, however, due to non-linearity of the target functional, we would have to perform an iterative optimization in order to find the optimal vector of weights $\mathbf{b}$ for the FIR filter.

2.2.3. Time domain least squares (tcfir)
This is the last approach from *cfir* family. It is based on minimization of the squared distance in the time domain between the complex delayed ground truth signal $y[n-D]$ and the filtered signal $x[n]^* b[n]$:

$$\mathbf{b}_{tcfir} = \arg\min_{\mathbf{b}} ||x[n] * b[n] - y[n-D]||_{L_2} \tag{12}$$

The ground truth signal $y[n-D]$ is obtained non-causally from the training samples via an ideal zero-phase Hilbert transformer (8). According to Parseval's theorem, this approach is equivalent to the *wcfir* approach. However in contrast to the frequency domain formulation, it allows for implementation of recursive schemes (12) and, therefore, may potentially account for non-stationarity in the data. One of the most straightforward solutions is to use recursive least squares [39] in order to update filter weights online.

2.3. Methods comparison

2.3.1. Data and preprocessing
We compared the performance of the methods described above using resting state EEG data recorded from ten participants engaged in neurofeedback experiments. Resting state data was collected prior to neurofeedback runs. Prior to the experiment, all participants provided written consent approved by The

Higher School of Economics Committee on Inter-University Surveys and Ethical Assessment of Empirical Research in accordance with the Declaration of Helsinki. EEG data was obtained using 32 AgCl electrodes placed according to the 10–20-system with the ground electrode at AFz position and reference electrodes on both ears. The impedance for all electrodes was kept below 10 KOhm. The signal was sampled at 500 Hz using an NVX-136 amplifier (Medical Computer Systems Ltd) and bandpass-filtered in the 0.5−70 Hz band. These *preprocessing* filters incurred an overall delay of no more than 10 milliseconds for the bandwidth of interest (8–12 Hz).

We used 2 minutes of resting state recordings for each participant. The first minute of the data was used for implementing a parametric grid search and the second minute - for performance testing. These processing steps corresponded to the settings of our neurofeedback experiments where, after recording a subject's resting state activity for one minute, we adjusted the signal processing parameters and then proceeded to the main body of the experiment. To eliminate eye artifacts, we performed independent component analysis (ICA) on the training data, identified eye movement-related components by means of the mutual information spectrum [40], and removed the artifactual data characterized by the highest mutual information with the two frontal channels Fp1 and Fp2. Only the parietal P4 channel of the cleaned data was used for the analysis and it played the role of $x[n]$ in (1).

2.3.2. Individual alpha band

We determined individual alpha ranges with the following procedure: estimate magnitude spectrum using Welch method with a 4 second 90%-overlap boxcar window, find the frequency f_0 with maximal signal-to-noise ratio (SNR) in the 8-12 Hz range, define individual band as $[f_1, f_2]$ interval, where $f_1 = f_0 - 2$ Hz and $f_2 = f_0 + 2$ Hz. SNR was defined as the difference between mean magnitude in the band $\Delta_{band} = [f_1, f_2]$ and mean magnitude in the flankers band $\Delta_{flankers} = [f_1 - 2, f_1] \bigcup [f_2, f_2 + 2]$ divided by the mean magnitude in the flankers band $\Delta_{flankers}$:

$$SNR = \frac{m(\Delta_{band}) - m(\Delta_{flankers})}{m(\Delta_{flankers})} \tag{13}$$

where $m(\Delta)$ is the mean magnitude in band Δ.

2.3.3. Ground truth signal

As the ground truth signal we used the non-causally computed analytic signal $y[n]$ obtained using the *ideal* procedure described in section 2 and illustrated in figure 2(A) and corresponding to the individual alpha band $[f_1, f_2]$ of each subject. After the analytic signal $y[n]$ was computed, we estimated both envelope and instantaneous phase without any additional delay according to equation (3).

2.3.4. Performance metrics

To measure the accuracy of the envelope and instantaneous phase estimation obtained with the described techniques, we used the following metrics. All metrics were based on the ground truth envelope and instantaneous phase information extracted from the ground truth signal $s[n]$ obtained non-causally from the real EEG data as described above and then shifted to match the specific delay value D of causal processing. We will denote the shifted ground truth envelope and phase sequences as $a[n-D]$ and $\phi[n-D]$ correspondingly.

To assess the performance of different methods for estimating the envelope, we calculated the Pearson correlation coefficient between the estimated envelope $\hat{a}[n]$, obtained causally with each of the methods, and the appropriately shifted ground truth envelope sequence $a[n-D]$ over the 1-minute long test data segment:

$$r_a = \frac{\sum_{n \in \mathcal{N}_a} (a[n-D] - m_a)(\hat{a}[n] - m_{\hat{a}})}{\sqrt{\sum_{n \in \mathcal{N}_a} (a[n-D] - m_a)^2} \sqrt{\sum_{n \in \mathcal{N}_a} (\hat{a}[n] - m_{\hat{a}})^2}} \tag{14}$$

where $\mathcal{N}_a = D \ldots N-1$ is the set of time indices with $N = 30000$, m_a and $m_{\hat{a}}$ are sample mean values of $a[n]$ and $\hat{a}[n]$ over set $\mathcal{N}_a$

To assess the performance of instantaneous phase estimation, we used bias b_ϕ, absolute bias $|b_\phi|$ and the standard deviation σ_ϕ with respect to the delayed ground truth phase $\phi[n-D]$ at the time when predicted $\hat{\phi}[n]$ phase crosses 0. These metrics reflect the bias, absolute bias, and the variance in determining zero crossings(negative-to-positive direction) of the delayed signal $s[n-D]$.

$$b_\phi = \frac{1}{|\mathcal{N}_\phi|} \sum_{n \in \mathcal{N}_\phi} \phi[n-D] \tag{15}$$

$$\sigma_\phi = \sqrt{\frac{1}{|\mathcal{N}_\phi| - 1} \sum_{n \in \mathcal{N}_\phi} (\phi[n-D] - b_\phi)^2} \tag{16}$$

where $\mathcal{N}_\phi = \{n : n \in \mathcal{N}_a,\ sign(\hat{\phi}[n]) > sign(\hat{\phi}[n-1])\}$ is the set of time instances when $\hat{\phi}[n]$ crosses 0.

2.3.5. Grid search procedure

To ensure that the methods being compared operated optimally, we defined a grid search space for each of them as described in table 1 and looked for the combination of parameters that ensured the best performance for each technique. Here we use the following short method names: *rect* for envelope detector based on rectification of the band-filtered signal, *cfir* for the frequency domain LSCF, *wcfir* for the frequency

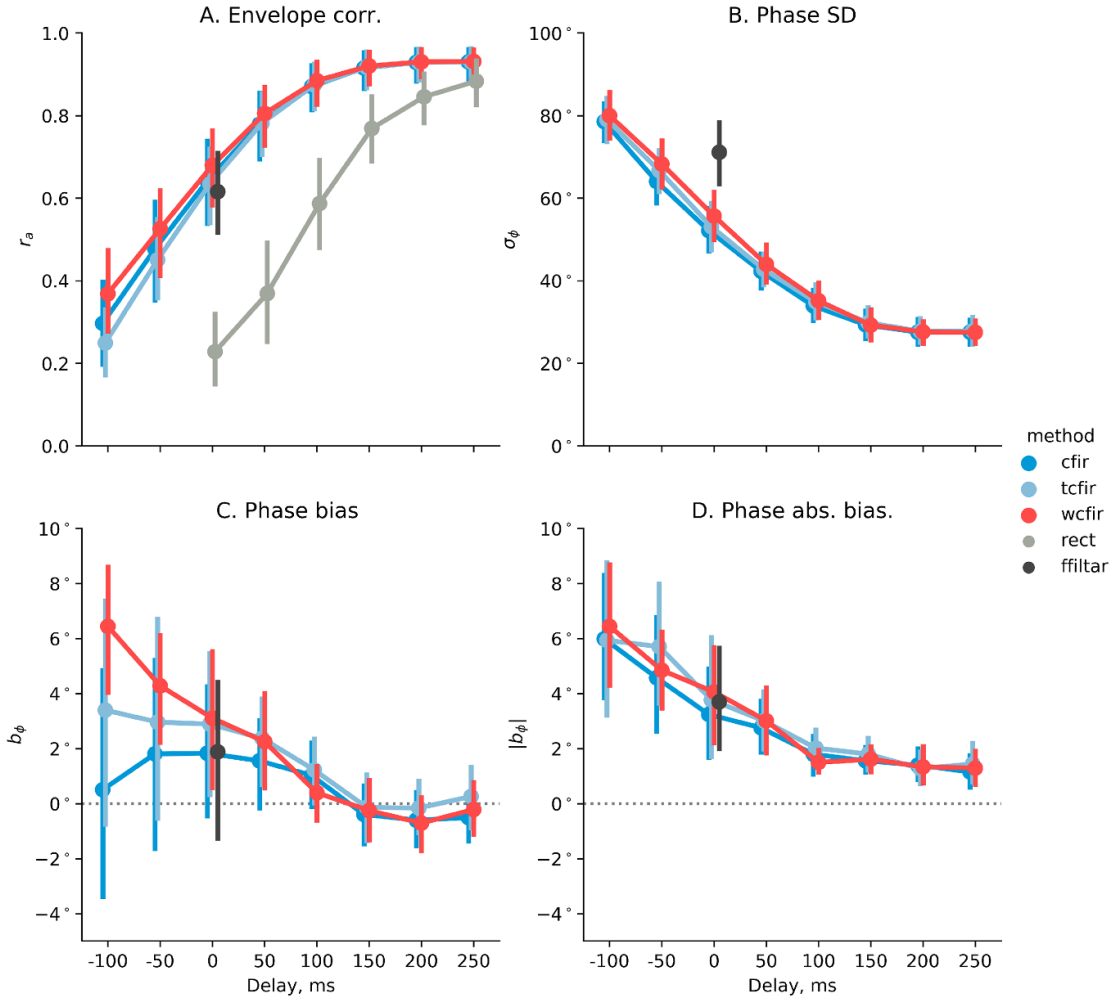

Figure 3. Four performance metrics vs incurred processing delay. (A) Dependence of the correlation coefficient r_a on delay D for the *cfir* family, for rectification based technique and AR-based extrapolation approach (*ffiltar*). (B) Phase estimation bias b_ϕ as a function of processing delay D. (C) Phase estimation variance σ_ϕ as a function of processing delay. (D) Phase estimation absolute bias $|b_\phi|$ vs. D.

domain weighted LSCF, *tcfir* for the recursive version of the LCSVF and *ffiltar* for the method based on autoregressive extrapolation of zero-phase filtered time series [33]. Note that when operating at a positive latency the sliding window narrow-band Hilbert transform approach (*hilb*) exactly matches the *cfir*.

For each combination of parameters and fixed delay D, we computed the metrics defined in equations (14–16) on the training set - separately for each subject. Note that no negative delay D is possible for *rect* and *hilb*, so we used only zero delay ($D = 0$) for *ffiltar*. The same approach was used in the closed-loop magnetic stimulation experiments in this specific condition [13, 33, 34] . Frequency band and weights for the *wcfir* approach were computed using the training data. We then used optimal parameters for each method corresponding to the maximum of r_a, minimum for $|b_\phi|$ and minimum of σ_ϕ values observed on the training set, and estimated the same performance metrics r_a, b_ϕ, $|b_\phi|$ and σ_ϕ on the test data.

We adjusted the filter weights and hyperparameters over the 1 minute segment of the resting state data recorded from the individual subject to ensure adequate performance of this filter during the entire course of recording (typically 15-20 minute). This adaptation makes the filter weights reflect individual shape of the alpha-peak and signal-to-noise (SNR) ratio of the occipital alpha oscillation. These parameters are specific to an individual and do not change over time. In practice, when needed the filter weights and the hyperparameters can be re-adjusted anytime using the most recent data segment.

3. Results

Figure 3 shows the comparison of different methods. The results are averaged over the data from ten participants. To ensure the best performance for each technique, we used training data segments to adjust each method's parameters using the grid search procedure described in the Methods section. For each

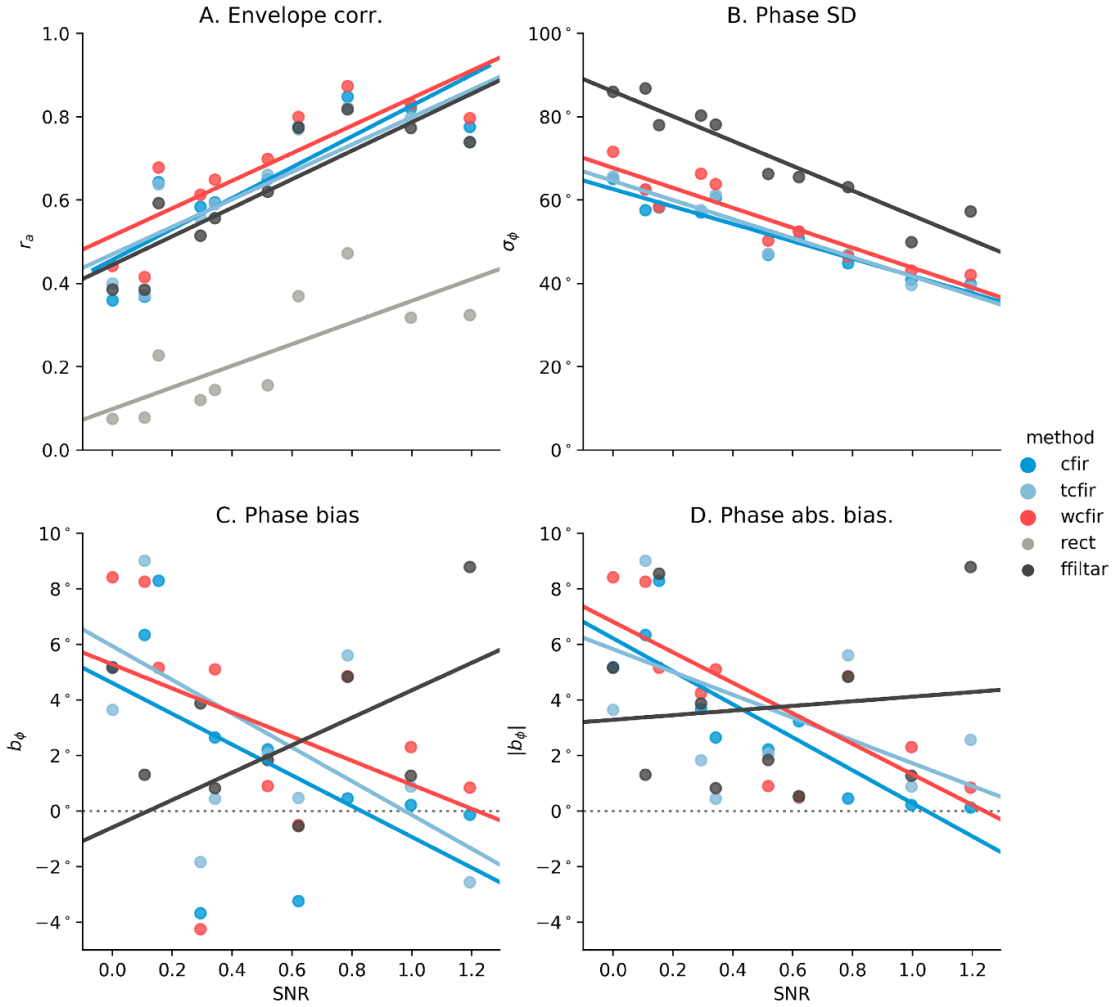

Figure 4. Four performance metrics vs. alpha rhythm SNR for D = 0. (A) Envelope correlation coefficient r_a, (B) Phase estimation standard deviation (SD) σ_ϕ and (C), (D) Phase estimation bias b_ϕ and absolute bias $|b_\phi|$. Each dot corresponds to a dataset and is positioned on the x-axis according to the P4 alpha-rhythm SNR.

Table 1. Grid search space for each method.

Method	Param.	Grid
rect	N_{bp}	0, 5, .., 100
cfir/*hilb*	N_t	250, 500, 1000
wcfir	N_t	250, 500, 1000
tcfir	N_t	250, 500, 1000
	N_u	25, 50
	μ	0.7, 0.8, 0.9
ffiltar	p	10, 25, 50
	N_e	10, 25, 50

method (panels A, B, C and D), we show the performance metrics r_a, σ_ϕ, b_ϕ, $|b_\phi|$ reflecting envelope correlation accuracy (panel A), phase estimate variance (panel B), phase estimate bias (panel C) and phase estimate absolute bias (panel D) as described by equations (14)–(16) and computed on the test data segment with the optimal set of parameters identified over the independent training data segment. For each such metric, the curves display the metric mean values averaged over ten participants as a function of the incurred delay. The error bars indicate the 95% confidence intervals obtained from 1000 bootstrap iterations. Our observations show that the accuracy metrics computed over 1 minute of the test data adequately reflects the average estimation accuracy exhibited over the entire duration of recording. Swapping the test and the train data results into qualitatively very similar relative performance curves.

Figure 3(A) shows that, as expected, the envelope estimation accuracy quantified by the correlation coefficient r_a deteriorates as the processing lag D decreases. The smaller the processing lag, the weaker is the correlation between the non-causally obtained ground-truth envelope and the envelope causally estimated by each of the methods. For all positive delays *rect* approach (gray line) has noticeably the worst performance making it practically unusable for latency values below 150 ms. Methods from the LSCF family, *cfir* (blue line), *wcfir* (red line) and *tcfir* (light blue line), exhibit comparable accuracy. The approach described in [33] (*ffiltar*, black dot) that entails autoregressive (AR) modeling of data and forward-backward filtering of the extended data chunk yields the accuracy comparable to that

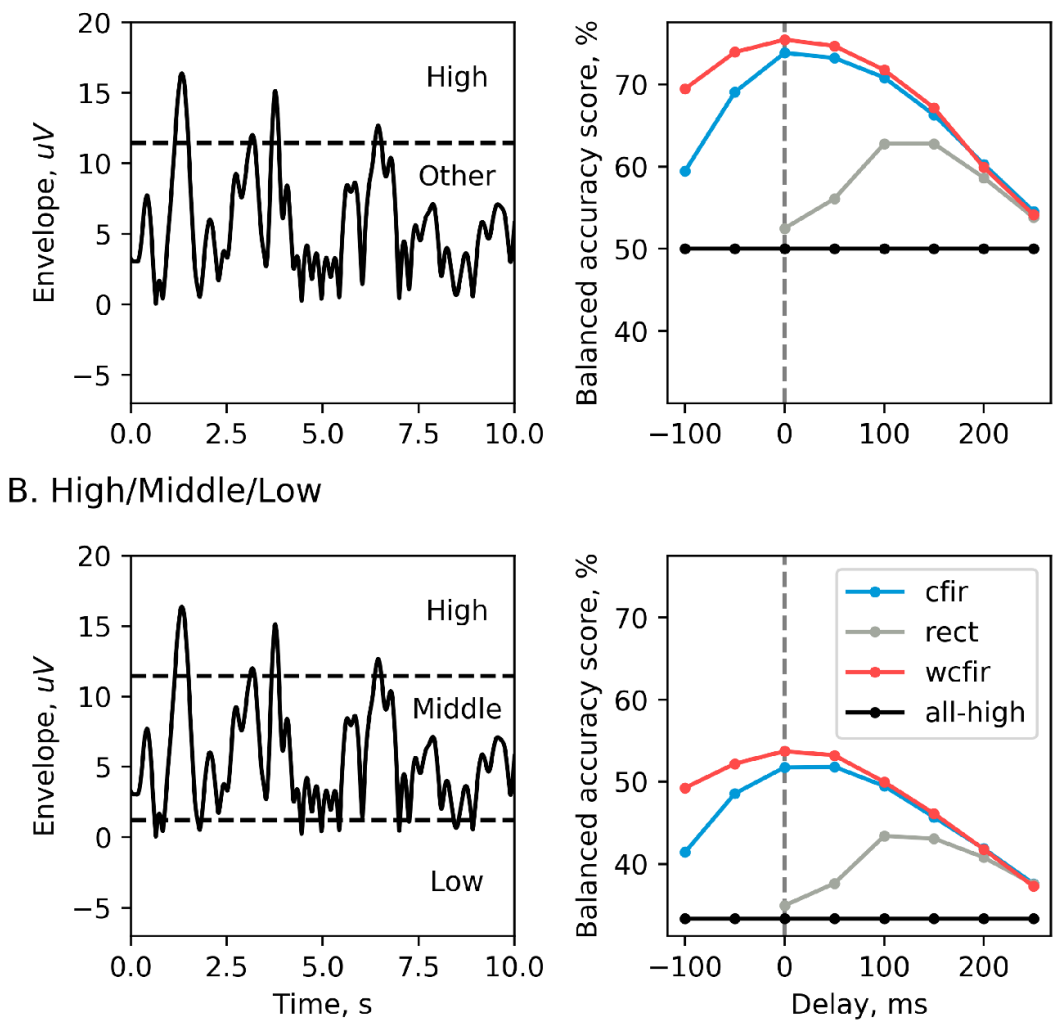

Figure 5. Discrete paradigm accuracy for one subject with median SNR. (A) Binary classification task. The goal is to detect the time instances when alpha envelope is in the upper 5% quantile of its values. (B) Ternary classification task to distinguish lower and upper 5% quantiles of the envelope values from the mid-range values falling into 5%–95% range.

delivered by the LSCF family of methods at zero latency but it also requires specification of parameters describing the AR model order, filter and extension window length, and it is significantly more computationally intense.

Panels B, C and D of figure 3 show the results for real-time estimation of instantaneous phase as a function of time-lag D. For the positive delay values, the bias b_ϕ remains practically negligible and does not exceed 5° for all considered methods. Noteworthy, the *ffiltar* approach formulated for zero-latency shows nearly zero mean phase estimation bias corresponding to $D = 0$. However, as panel D demonstrates, the absolute bias of the phase estimate obtained by this technique is comparable to that delivered by the LSCF family of methods. Therefore, the close-to-zero average phase estimation bias in panel C reflects symmetry around zero distribution of phase estimation bias values observed in the ten examined datasets. The methods from the LSCF family exhibit a significant growth of phase estimation standard deviation (SD) as lag D decreases. Yet, at zero lag, the variance of the estimate delivered by the proposed family of techniques appears to be significantly below that of the *ffiltar* approach. Here we reported an averaged observations made on the basis of the data recorded from ten participants as described in section 2.3.

Considering each subject separately allowed us to explore the performance as a function of the SNR that naturally varied across individuals. Figure 4 illustrates the same three performance measures as shown in figure 3 for individual participants but only for $D = 0$.

Figure 4 shows the performance of the explored methods for $D = 0$ as a function of the SNR observed in each of the individual subjects. Metrics of the performance are the same as in figure 3. For all methods, envelope correlation r_a grows with the SNR, panel A. SD of the estimated phase improves with SNR and appears to be consistently lower for the LSCF family of methods. Phase estimate bias b_ϕ shows positive skew

for the low SNR value. The absolute bias for *ffiltar* technique appears to be independent of the SNR. For high SNR values starting with 1.0 the absolute bias value obtained by all methods from the LSCF family appears to be consistently lower than that of the *ffiltar*. Also for the LSCF family we observe the expected reduction in the bias of the estimated phase with the growth of the SNR. Although not significantly, in the envelope estimation task the *wcfir* approach always performs slightly better than the other methods. This method takes into account the spectral peak shape which may bring more benefits to the real-time quantification of brain rhythms with larger bandwidth, e.g. beta and gamma rhythms. Recursive least squares (RLS) based *tcfir* approach is designed to accommodate non-stationarities of the brain rhythm's spectral characteristics. However, in the application where alpha oscillations were monitored this approach does not render any advantage over the stationary methods pre-trained on the 1 minute long segment of preceding data. To make sure that these observations were invariant to the arrangement of the *test* and *train* segments, we computed the performance graphs for the data where the test and train segments were swapped. This test yielded the same trends as shown in figures 3 and 4.

A full-blown envelope reconstruction is not required in some versions of the closed-loop paradigms e.g. [17]. Instead, of interest is the discrete detection of time instances with high instantaneous within-band amplitude. Crossing the prespecified threshold by the rhythm's envelope may serve as a feedback or a trigger to either present a stimulus or directly stimulate brain. Suppose we want to perform detection of the time when the instantaneous rhythm power exceeds the 95% threshold. As shown in the left panel of figure 5(A), for the binary classification case, the time instance when the envelope crosses the threshold (dashed line) are labeled as *High*, and the rest of the moments are labeled as *Low*. The right panel of figure 5(A) shows the balanced accuracy score (class recall average) for such binary detection task as a function of the allowed processing delay parameter D. The analysis is done for one participant with median SNR selected from the pull of ten participants. We can observe that the best performance in the binary classification task is achieved by the weighted *cfir* method with zero processing latency ($D = 0$). Similar results for ternary classification of the three-state problem are shown in figure 5(B). Just like in the binary case, the instances when the envelope falls into the top area corresponding to the 5% of the largest envelope values are labeled as *High* and additionally, label *Low* is assigned to the time instances when the envelope takes on values from the lowest 5%. The rest of the time instances are labeled as *Medium*. As in the binary classification test, the weighted version of the *wcfir* approach delivers the best performance for zero processing delay $D = 0$. In the binary classification scenario, we can achieve about 75% of balanced accuracy. The rectification-based approach is unable to operate at such a short latency and it yields just above 60% maximal accuracy even with 100–150 ms delay. Similar conclusion can be drawn from the ternary classification case results.

Finally, to explore the shape of the alpha-burst events in the *High*/*Other* classification task described above in figure 6, we averaged the ground truth envelope triggered on the crossings of the threshold. This computation was performed for *rect* and *wcfir* approaches for predefined delay parameters from $[300, 100, 0, -100]$ ms set (for *rect* only positive values were used). Also, we computed an average envelope across a set of randomly picked time moments (denoted as *rand*) and across the instances when the *ground truth* envelope crossed the *High* threshold (denoted as *ideal*), which can not be done causally, see figure 6.

Figure 6 shows that the averaging of the alpha band envelope profiles around the time instances detected using the *wcfir* approach operating at $D = 0$ ms latency results into a well pronounced peak that practically coincides with $t = 0$. Therefore, the feedback signal sent at the time instances detected with *wcfir* will arrive when alpha power is elevated and not past this event. At the same time, the negative delay only slightly improves the detection latency but increases the variance which is not the desirable behavior.

4. Discussion

Standard techniques for estimating instantaneous power of EEG rhythms, such as the methods based on the rectification of narrow-band filtered signal and the STFT based algorithms, incur significant delays, which hinders the performance in BRCPs. Such delays, combined with the lags of acquisition hardware and the time required for stimulus presentation, result in significant lags between the actual brain activity and the signal used to control the experimental flow in the BRC paradigms. In the closed-loop stimulation paradigms, this would mean that the timing of the stimulating pulse can not be accurately aligned to the desired feature of the oscillatory brain activity. In the neurofeedback setting or settings requiring an explicit feedback signal that reflects subject's performance, these standard approaches close the loop more than 300 ms past the targeted neural event [27]. Such delays may be especially detrimental when the targeted brain rhythm patterns can be described as discrete events of a limited duration [7], [41], [42] where the feedback can arrive after the event has completed. Such low temporal specificity of the feedback signal hinders learning, especially in the automatic learning scenarios [28]. Here we systematically explored a series of methods for minimizing latency in BRCPs. We distinguished a family

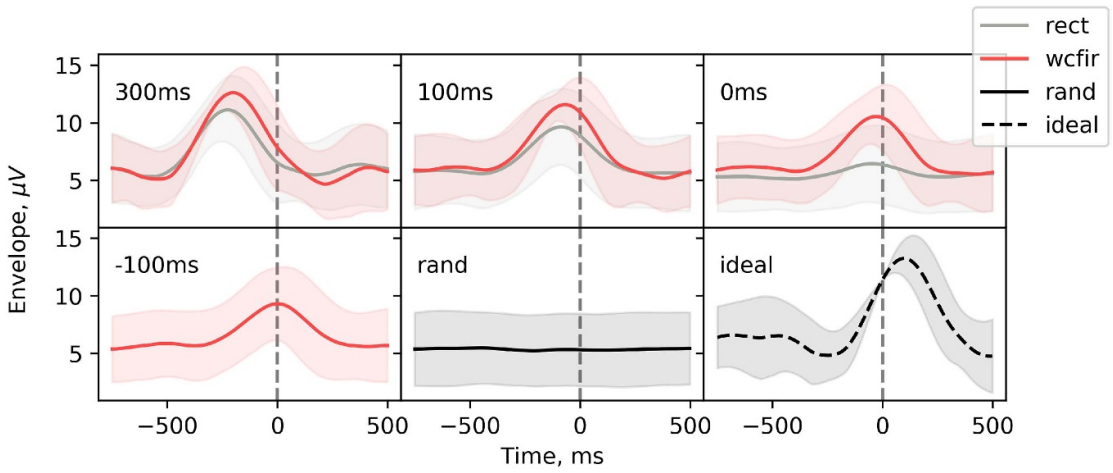

Figure 6. Average envelope computed using real-time detected markers of *High* events for different pre-specified processing delay values.

of best-performing techniques that are based on the least-squares complex-valued FIR filter design. These methods allow for a simpler and more transparent control over the speed–accuracy trade-off compared to the other existing approaches.

Our results confirm that the methodology based on the least-squares complex-valued filter design noticeably reduces latency of EEG envelope and phase estimation. The computational procedure is simple; yet its efficiency pars or exceeds that of the more complex approaches, including those based on the use of the AR-model [33] - the most ubiquitous method for closed-loop studies [43], [13], [34], [44]. Using our method, one can specify the desired delay and achieve the best possible envelope estimation accuracy possible with a linear method. As evident from figure 3, *wcfir* technique allowed us to generate zero-latency feedback that accurately tracked the instantaneous power profile of the EEG-rhythm. The performance of the proposed approach on a typical segment of data can be appreciated from figure 7 which shows true values and estimates of the envelope and phase obtained with *wcfir* method for various user specified lags.

The methods in the LSCF family slightly differ in their properties and expected applicability. The simplest *cfir* approach performs on par with the more advanced *wcfir* technique when used to estimate alpha-band envelope. However, *wcfir* appears to have advantages in the discrete task of detecting threshold crossing by the rhythm's envelope. It adapts to the shape of the spectrum within the band of interest and thus may have advantages over the *cfir* approach, especially when dealing with the real-time quantification of brain rhythms with larger bandwidth, e.g. beta and gamma rhythms. Non-stationary *tcfir* may be useful when the rhythm properties are likely to change over time as it can be the case in neurofeedback training experiments or when the experiments explicitly imply several states of the participants, e.g. eyes-open and eyes-closed states characterized by different properties of rhythmic activity.

This work is a part of our systematic effort aimed at building a zero- or even negative-latency feedback paradigm that will allow transferring the predictive control methodology successfully exercised in technical systems to the tasks where the brain is the controlled object [45]. As shown in 5, the *wcfir* provide for correct instantaneous detection of rhythmic activity bursts, with AUC exceeding 75%. This illustration suggests that the proposed family of simple approaches together with the necessary hardware optimization will open up avenues for the implementation of low-latency feedback scenarios and enable a more efficient interaction with brain circuits.

Fundamentally, the reduced feedback latency comes at a cost of a less accurate envelope estimation. Deterioration of performance is especially sizeable when the SNR is low and therefore, for the latency-reduction algorithm to be efficient, care should be taken to improve the SNR with such methods as spatial filtering of multi-electrode recordings. Joint spatial-temporal filters aimed at extracting the analytic signal with the user specified delay may potentially harness the power of the complex EEG dynamics to further improve the rhythmic components quantification accuracy. The optimal speed-accuracy trade-off is the issue that needs to be addressed for each application and each participant individually. As shown in figure 3, the methods outlined in this work allow for a smooth control of this trade-off and a choice of an optimal operational point for an individual application.

As mentioned above, to achieve a true predictive scenario, the signal processing algorithms need to be improved, but the hardware employed for

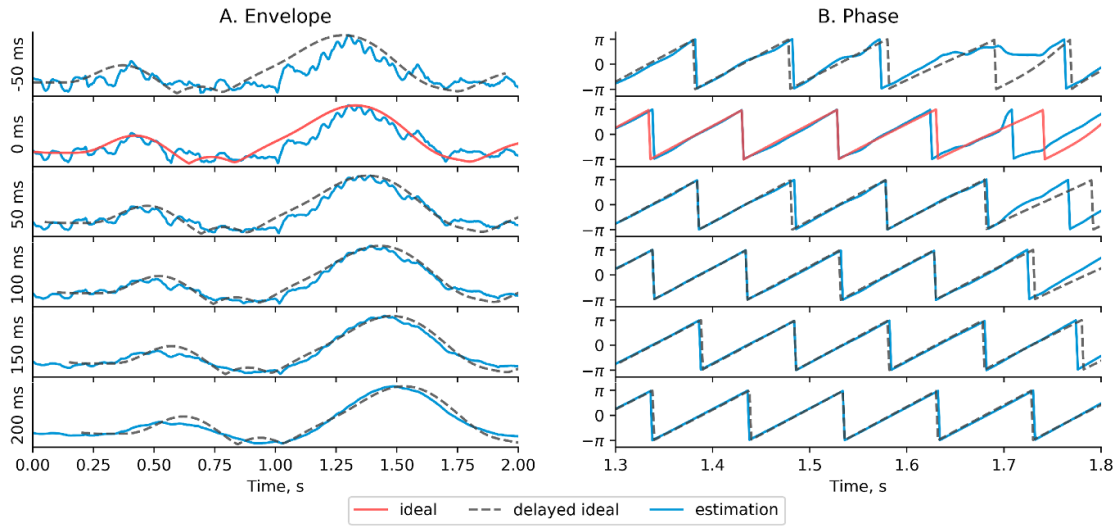

Figure 7. Envelope (A) and phase (B) estimates obtained by *wcfir* method (blue line) for different delay values *D*. Each row corresponds to delays from −50 ms to 200 ms. Red line denotes ground-truth signal calculated by the ideal non-causal filter, gray dashed line denotes the same ground-truth signal but shifted by the corresponding delay *D* to facilitate comparison.

signal acquisition as well as the low-level software that handles EEG data transfer from the acquisition device to the computer memory buffer need to be improved too. To this end, it is worth considering specialized systems based on the Field-Programmable Gate Array (FPGA) devices that eliminate the uncertain processing delays present in computer operating systems not designed to operate in real-time [46].

In the context of neurofeedback, additional consideration should be given to the physiological aspects of the sensory modality used to deliver the feedback signal. For instance, visual inputs, although very informative [31], are processed slower as compared to the tactile inputs; therefore, tactile feedback could be a better option for short-latency control. A combination of modalities can also be considered as a way to improve performance. For example, in the context of alpha-band neurofeedback training short-latency tactile or audio feedback could be used to reinforce the participant when alpha-band envelope crosses a prespecified threshold and the screen could demonstrate the accumulated count of such cases.

The signal processing approaches presented here could be advanced by employing more sophisticated decision rules capable of extracting hidden structures from the data. Thus, convolutional neural networks [47], [48] and novel recursive architectures hold a significant promise to further improve the accuracy of real-time zero-lag envelope and phase estimation.

5. Reproducibility

The code implementing all the described methods is available at https://github.com/nikolaims/cfir including all the necessary links to the data to reproduce the results reported in the paper.

Acknowledgments

This work is supported by the Center for Bioelectric Interfaces NRU HSE, RF Government grant, ag. No.14.641.31.000 3. We also thank Dr Maria Volodina and Dr Andriy Myachykov for the careful proofread of the final version of this manuscript.

ORCID iDs

Nikolai Smetanin
https://orcid.org/0000-0001-8178-1598
Alexei Ossadtchi
https://orcid.org/0000-0001-8827-9429

References

[1] Buzsáki G 2009 *Rhythms of The Brain* (Oxford: Oxford University Press)
[2] Nunez P L and Srinivasan R 2006 *Electric Fields of the Brain: The Neurophysics of EEG* (Oxford: Oxford University Press)
[3] Zrenner C, Belardinelli P, Müller-Dahlhaus F and Ziemann U 2016 Closed-loop neuroscience and non-invasive brain stimulation: A tale of two loops *Front. Cell. Neurosci.* **10** 92
[4] Sterman M, MacDonald L and Stone R K 1969 Operant control of the EEG alpha rhythm and some of its reported effects on consciousness *Altered States of Consciousness*
[5] Sterman M, MacDonald L and Stone R K 1974 Biofeedback training of the sensorimotor electroencephalogram rhythm in man: effects on epilepsy *Epilepsia* **15** 395–416
[6] Sitaram R *et al* 2016 Closed-loop brain training: the science of neurofeedback *Nat. Rev. Neurosci.* **18** 86–100
[7] Ossadtchi A, Shamaeva T, Okorokova E, Moiseeva V and Lebedev M 2017 Neurofeedback learning modifies the incidence rate of alpha spindles, but not their duration and amplitude *Sci. Rep.* **7** 3772
[8] Wolpaw J *et al* 2012 *Brain Computer Interfaces: Principles and Practice* (Oxford: Oxford University Press)
[9] Frolov A, Kozlovskaya I, Biryukova E and Bobrov P 2017 Robotic devices in poststroke rehabilitation *Zhurnal Vysshei Nervnoi Deyatelnosti Imeni I.P. Pavlova*

[10] Ang K K, Chua K S, Phua K S, Wang C, Chin Z Y, Kuah C W, Low W and Guan C A 2015 Randomized controlled trial of EEG-based motor imagery brain-computer interface robotic rehabilitation for stroke *Clin. EEG Neurosci.* **46** 310–20
[11] Hady A E 2016 *Closed Loop Neuroscience* (Amsterdam: Elsevier)
[12] Bergmann T O, Karabanov A, Hartwigsen G, Thielscher A and Siebner H R 2016 Combining non-invasive transcranial brain stimulation with neuroimaging and electrophysiology: Current approaches and future perspectives *NeuroImage* **140** 4–19
[13] Schaworonkow N, Zrenner C, Triesch J and Ziemann U 2019 EEG-triggered TMS reveals stronger brain state-dependent modulation of motor evoked potentials at weaker stimulation intensities *Brain Stimul.* **12** 110–18
[14] Nokia M S and Wikgren J 2014 Effects of hippocampal state-contingent trial presentation on hippocampus-dependent nonspatial classical conditioning and extinction *J. Neurosci.* **34** 6003–10
[15] Mazaheri A, van Schouwenburg M R, Dimitrijevic A, Denys D, Cools R and Jensen O 2014 Region-specific modulations in oscillatory alpha activity serve to facilitate processing in the visual and auditory modalities *NeuroImage* **87** 356–62
[16] Zumer J M, Scheeringa R, Schoffelen J-M, Norris D G and Jensen O 2014 Occipital alpha activity during stimulus processing gates the information flow to object-selective cortex *PLoS Biol.* **12** e1001965
[17] Samaha J, Iemi L and Postle B R 2017 Prestimulus alpha-band power biases visual discrimination confidence, but not accuracy *Conscious. Cogn.* **54** 47–55
[18] Kaiser M, Senkowski D, Busch N A, Balz J and Keil J 2019 Single trial prestimulus oscillations predict perception of the sound-induced flash illusion *Sci. Rep.* **9** 5983
[19] Hanslmayr S, Aslan A, Staudigl T, Wolfgang K, Herrmann C S and Bäuml K-H 2007 Prestimulus oscillations predict visual perception performance between and within subjects *NeuroImage* **37** 1465–73
[20] Rahmandad H, Repenning N and Sterman J 2009 Effects of feedback delay on learning *Syst. Dynamics Rev.* **25** 309–38
[21] Lofthouse N, Hendren R, Hurt E, Arnold L E and Butter E 2012 A review of complementary and alternative treatments for autism spectrum disorders *Autism Res. Treat.* **2012** 870391
[22] Coben R, Linden M and Myers T E 2010 Neurofeedback for autistic spectrum disorder: a review of the literature *Appl. Psychophysiol. Biofeedback* **35** 83–105
[23] Zoefel B, Huster R J, and Herrmann C S 2011 Neurofeedback training of the upper alpha frequency band in EEG improves cognitive performance *Neuroimage* **54** 1427–31
[24] Grosse-Wentrup M, Mattia D and Oweiss K 2011 Using brain–computer interfaces to induce neural plasticity and restore function *J. Neural Eng.* **8** 025004
[25] van Ede F, Quinn A J, Woolrich M W and Nobre A C 2018 Neural oscillations: Sustained rhythms or transient burst-events? *Trends Neurosci.* **41** 415–17
[26] Andermann M L, Jaakko Kaki, Tapio Paki, Moore C I, Riitta H, Jääskeläinen I P and Mikko S 2012 Brain state-triggered stimulus delivery: An efficient tool for probing ongoing brain activity *Open J. Neurosci.* 2 5
[27] Sherlin L H, Arns M, Lubar J, Heinrich H, Kerson C, Strehl U and Barry Sterman M 2011 Neurofeedback and basic learning theory: Implications for research and practice *J. Neurother.* **15** 292–304
[28] Lacroix J M 1986 *Mechanisms of Biofeedback Control* (Boston, MA: Springer)
[29] Grice G R 1948 The relation of secondary reinforcement to delayed reward in visual discrimination learning *J. Exp. Psychol.* **38** 1–16
[30] Kitazawa S, Kohno T and Uka T 1995 Effects of delayed visual information on the rate and amount of prism adaptation in the human *J. Neurosci.* **15** 7644–52
[31] Evans N, Gale S, Schurger A and Blanke O 2015 Visual feedback dominates the sense of agency for brain-machine actions *PLoS ONE* **10** e0130019
[32] Oblak E F, Lewis-Peacock J A and Sulzer J S 2017 Self-regulation strategy, feedback timing and hemodynamic properties modulate learning in a simulated fMRI neurofeedback environment *PLoS Comput. Biol.* **13** e1005681
[33] Chen L L, Madhavan R, Rapoport B I and Anderson W S 2013 Real-time brain oscillation detection and phase-locked stimulation using autoregressive spectral estimation and time-series forward prediction *IEEE Trans. Biomed. Eng.* **60** 753–62
[34] Schaworonkow N, Gordon P C, Belardinelli P, Ziemann U, Bergmann T O and Zrenner C 2018 μ-rhythm extracted with personalized EEG filters correlates with corticospinal excitability in real-time phase-triggered EEG-tms *Front. Neurosci.* **12** 954
[35] Oppenheim A V and Schafer R W 2010 *Discrete-Time Signal Processing* 3rd edn (Englewood Cliffs, NJ: Prentice-Hall)
[36] Bruns A 2004 Fourier-, Hilbert- and wavelet-based signal analysis: are they really different approaches? *J. Neurosci. Methods* **137** 321–32
[37] Voytek B, Kayser A S, Badre D, Fegen D, Chang E F, Crone N E, Parvizi J, Knight R T and D'Esposito M 2015 Oscillatory dynamics coordinating human frontal networks in support of goal maintenance *Nat. Neurosci.* **18** 1318–24
[38] Lee W R, Caccetta L, Teo K L and Rehbock V 2006 Optimal design of complex FIR filters with arbitrary magnitude and group delay responses *IEEE Trans. Signal Process.* **54** 1617–28
[39] Haykin S 2002 *Adaptive Filter Theory* (Englewood Cliffs, NJ: Prentice-Hall)
[40] Ossadtchi A, Pronko P, Baillet S, Pflieger M E and Stroganova T 2014 Mutual information spectrum for selection of event-related spatial components. application to eloquent motor cortex mapping. *Front. Neuroinform.* **7** 53
[41] Shin H, Law R, Tsutsui S, Moore C I and Jones S R 2017 The rate of transient beta frequency events predicts behavior across tasks and species *Elife* **6** e29086
[42] Sherman M A, Lee S, Law R, Saskia H, Catherine A T, Matti S Hamäläinen, Moore C I and Stephanie R J 2016 Neural mechanisms of transient neocortical beta rhythms: Converging evidence from humans, computational modeling, monkeys, and mice *Proc. Natl Acad. Sci.* 113 E4885–E4894
[43] Zrenner C, Desideri D, Belardinelli P and Ziemann U 2018 Real-time EEG-defined excitability states determine efficacy of TMS-induced plasticity in human motor cortex *Brain Stimul.* **11** 374–89
[44] Jianguang N, Wunderle T, Lewis C M, Desimone R, Diester I and Fries P 2016 Gamma-rhythmic gain modulation *Neuron* **92** 240–51
[45] Liu Y-Y and Barabási A-L 2016 Control principles of complex systems *Rev. Mod. Phys.* **88** 035006
[46] Wöhrle H, Tabie M, Kim S, Kirchner F and Kirchner E 2017 A hybrid FPGA-based system for EEG- and EMG-based online movement prediction *Sensors* **17** 1552
[47] Schirrmeister R T, Springenberg J T, Fiederer L, Glasstetter M, Eggensperger K, Tangermann M, Hutter F, Burgard W and Ball T 2017 SelDeep learning with convolutional neural networks for EEG decoding and visualization *Hum Brain Mapp* **38** 5391–420
[48] Zubarev I, Zetter R, Halme H L and Parkkonen L 2019 Adaptive neural network classifier for decoding meg signals *Neuroimage* **197** 425–34